JGR Planets

RESEARCH ARTICLE
10.1029/2024JE008525

# Equation of State, Structure, and Transport Properties of Iron Hydride Melts at Planetary Interior Conditions

**Emma R. Stoutenburg[1], Razvan Caracas[2,3], Natalia V. Solomatova[4], and Andrew J. Campbell[1]**

[1]Department of the Geophysical Sciences, University of Chicago, Chicago, IL, USA, [2]Université Paris Cité, Institut de Physique du Globe de Paris, CNRS, Paris, France, [3]The Center for Planetary Habitability (PHAB), University of Oslo, Oslo, Norway, [4]Laboratoire de Géologie de Lyon LGLTPE UMR5276, CNRS, Ecole Normale Supérieure de Lyon, Centre Blaise Pascal, Lyon, France

**Key Points:**

- Iron and hydrogen diffuse more rapidly and melts become less viscous at higher hydrogen concentrations
- The addition of hydrogen causes molar volume to decrease while compressibility and thermal expansivity increase
- Molecular hydrogen bonds increase with hydrogen concentration, and molecular hydrogen remains dissolved in the metallic melt

**Supporting Information:**

Supporting Information may be found in the online version of this article.

**Correspondence to:**

E. R. Stoutenburg,
estoutenburg@uchicago.edu

**Citation:**

Stoutenburg, E. R., Caracas, R., Solomatova, N. V., & Campbell, A. J. (2024). Equation of state, structure, and transport properties of iron hydride melts at planetary interior conditions. *Journal of Geophysical Research: Planets*, *129*, e2024JE008525. https://doi.org/10.1029/2024JE008525

Received 31 MAY 2024
Accepted 20 SEP 2024



**Abstract** Iron hydrides are a potentially dominant component of the metallic cores of planets, primarily because of hydrogen's ubiquity in the universe and affinity for iron. Using ab initio molecular dynamics, we examine iron hydrides with 0.1, 0.33, 0.5, and 0.6 mol fraction hydrogen up to 100 GPa between 3,000 and 5,000 K to describe how hydrogen content affects the melt structure, hydrogen speciation, equation of state (EOS), atomic diffusivity, and melt viscosity. We find that the addition of hydrogen decreases the average Fe–Fe coordination number and lengthens Fe–Fe bonds, while Fe–H coordination number increases. The pair distribution function of hydrogen at low pressure indicates the presence of molecular hydrogen. By tracking chemical speciation, we show that the amount of molecular hydrogen increases and the number of iron in $H_{x\geq1}Fe_{y\geq0}$ clusters decreases as the hydrogen concentration increases. We parameterize a pressure, volume, temperature, and composition EOS and show that the molar volume and Grüneisen parameter of the melts decrease while the compressibility and thermal expansivity increase as a function of hydrogen concentration. We find that hydrogen acts as a lubricant in the melts as the iron and hydrogen become more diffusive and the melts become more inviscid as the hydrogen concentration increases. We estimate 2.7 wt% hydrogen in the Martian core and 0.49–1.1 wt% hydrogen in Earth's outer core based on comparisons to seismic models, with the assumption that the cores are pure liquid iron-hydrogen alloy, and we compare the small exoplanet population with mass-radius curves of iron hydride planets.

**Plain Language Summary** Hydrogen, the most abundant element in the universe, is important to consider as a potential alloying element in the iron-rich cores of planets. We use advanced quantum mechanical methods to simulate molten iron hydrides from 10 to 60 atomic % hydrogen at the high pressures and temperatures in planetary interiors. We show that increasing hydrogen concentration causes the iron-iron bond distance to increase, iron-iron coordination number to decrease, and iron-hydrogen coordination number to increase. Futher, the speciation of hydrogen changes from almost purely atomic to partially molecular, while remaining dissolved in iron. We find that the more hydrogen is in the melt, the higher the diffusivity of the atoms and the lower the viscosity. We fit an equation of state to describe the relationship between pressure, volume, temperature, and hydrogen concentration, and show that the addition of hydrogen lowers molar volume and increases the compressibility and thermal expansivity in the melts. Based on our equation of state, if the outer core of Earth and the core of Mars were pure, liquid iron-hydrogen alloys, they would contain 0.49–1.1 and 2.7 weight% hydrogen, respectively.

## 1. Introduction

The cores of terrestrial planets consist primarily of iron-nickel alloy with some enrichment in lighter elements, which lower the core's density relative to pure iron. Hydrogen is particularly important to consider as a component of Earth's and other bodies' cores because of its cosmochemical abundance. Realistically, a mélange of light elements, including hydrogen, oxygen, sulfur, silicon, and carbon, could exist in Earth's core as well as a proportion of nickel, all of which will influence the physical properties of the metal. The characterization of relatively simple binary and ternary iron alloys is an important stepping stone to understanding how light elements affect the properties of the iron alloys (Hirose et al., 2021).

Hydrogen's siderophility (i.e., preference for metallic phases over silicate phases) has been demonstrated at pressures as low as 3.8 GPa and temperatures under 1,000 K, implying that even small, differentiated bodies such

as planetesimals could have hydrogen-enriched cores (Iizuka-Oku et al., 2017). Hydrogen's siderophility is enhanced with pressure, meaning larger bodies can accommodate a higher proportion of hydrogen in their cores than their mantles compared to small bodies (Tagawa et al., 2021; Yuan & Steinle-Neumann, 2020). Thus, if present, the hydrogen in a planet's interior could partition mostly into the core (Iizuka-Oku et al., 2017; Li et al., 2020; Okuchi, 1997; Suzuki et al., 1984; Tagawa et al., 2021; Yuan & Steinle-Neumann, 2020).

Hydrogen can be introduced to planetary interiors and the iron-rich cores of these bodies in several ways. Inside the snowline of a solar system, the accretionary material is mostly dry, but these mineral grains may absorb hydrogen directly from the solar nebula (Stimpfl et al., 2006) or may agglomerate with hydrous dust that drifts from beyond the snowline (Ciesla & Lauretta, 2005). Beyond the snowline, planet-building materials can contain significant numbers of hydrogen-bearing minerals. Hydrogen can also be delivered to the inner disk by impactors from beyond the snowline during accretionary growth (O'Brien et al., 2014; Raymond et al., 2009). There is evidence that an atmosphere of Solar composition was in-gassed through the magma ocean on Earth, potentially introducing tons of hydrogen to the interior of the planet (Broadley et al., 2022; Jaupart et al., 2017). If a planet accretes sufficient mass to capture an atmosphere before the dissipation of the hydrogen-dominated solar nebula, in-gassing through the magma ocean-atmosphere interfaces may be a common process in the Galaxy (Olson & Sharp, 2019; Young et al., 2023).

Despite the potential for iron-rich cores to host significant hydrogen, iron hydride melts at high pressure and temperature have received relatively little attention experimentally (compared to other iron-light element compounds) due to difficulties in both in situ and ex situ high-pressure and high-temperature experimental analyses. Liquid phases lack X-ray diffraction peaks, so the volume of a melt, and thus its composition, is not easily measurable in situ and when it is calculated, it can be imprecise. Hydrogen-rich melts, in particular, introduce problems: hydrogen easily diffuses into and causes critical failure of diamond anvils in high-pressure and high-temperature experiments. Furthermore, since hydrogen is insoluble in iron at ambient conditions (Fukai & Suzuki, 1986), it escapes a quenched iron melt upon decompression such that the composition of a high-pressure iron hydride melt cannot be measured upon sample recovery. This also means that composition is difficult to control during experiments, as iron hydrides of certain hydrogen concentrations cannot be synthesized easily at ambient conditions and then loaded as samples like other iron-light element alloys can be. Early experimental work on iron hydride melts is largely qualitative, proving that reactions take place based on textures of recovered samples but not reliably estimating the precise composition of the iron hydrides (Okuchi, 1997; Suzuki et al., 1984). In situ X-ray diffraction studies are more quantitative, but they assume the hydrogen concentration of the melt to be equivalent to what is measured in the solid quench product (Hirose et al., 2019; Oka et al., 2022; Tagawa et al., 2021). This is because, in solid phases, the composition of an iron hydride can be measured based on the volumetric deviation of the observed phase from that of pure iron (Caracas, 2015; Hirose et al., 2019; Thompson et al., 2018). However, hydrogen could be more soluble in liquid than in solid, meaning the true liquid composition may be more hydrogen-rich than what is measured in the quench product, with the hydrogen partitioning out of the quench phase aided by its high diffusivity. Overall, experimental work on molten iron hydrides is hindered by the unique challenges that hydrogen poses.

Contrary to experiments, ab initio molecular dynamics (AIMD) simulations allow direct and precise characterizations of high-pressure, high-temperature iron hydride fluids, so that their properties can be obtained as a function of their hydrogen concentration. Several AIMD studies focus on iron hydride melts, especially in the context of the Earth's outer core (130–330 GPa, 4,000+ K). Umemoto and Hirose (2015) simulated 0.22–0.41 mol fraction hydrogen in iron at 100–330 GPa and 4,000–7,000 K and identified the upper-bound hydrogen content in the Earth's outer core to be ∼1 wt% based on comparisons of their iron hydrides' properties with the Preliminary Reference Earth Model (PREM, Dziewonski & Anderson, 1981). Li et al. (2022) showed that $Fe_{0.91}H_{0.09}$ at 135 and 330 GPa and 4,500–7,000 K has low viscosity, like pure iron, and that the addition of hydrogen makes iron more diffusive.

Posner and Steinle-Neumann (2019) and Ohmura et al. (2020) studied molten iron hydrides amongst a suite of other binary iron-light element alloys. Posner and Steinle-Neumann (2019) modeled iron alloys with 0.04 mol fraction of hydrogen over a wide range of densities, corresponding to pressures of a few gigapascals up to the pressure conditions of the Earth's outer core between 2,500 and 6,500 K. They show that hydrogen occupies interstices in the iron melt, the iron-iron coordination is not strongly affected relative to pure iron, and that iron's diffusivity is about 1.6 times slower than pure iron. Ohmura et al. (2020) simulated 0.1–0.3 mol fractions of

hydrogen in iron at 140 GPa and 5,000 K and showed that hydrogen self-interaction is negligible compared to that of carbon, oxygen, silicon, and sulfur in binary iron alloys. They also find that hydrogen exists in the iron melt interstitially, as do carbon and oxygen; by contrast, sulfur and silicon substitute for iron. They also find that of all the hydrogen-light element alloys investigated, hydrogen decreases the molar volume the most.

In this work, we simulate liquid iron hydrides with a mole fraction of hydrogen $X = 0.1$–$0.6$ up to 100 GPa and 5,000 K using AIMD to describe how iron hydride melts evolve as a function of hydrogen concentration, pressure, and temperature. In addition to studying higher hydrogen concentrations than previous studies, we study conditions relevant to pressure- and temperature-conditions outside the Earth's outer core, including the early Earth, Earth's mantle, and smaller planetary bodies. These conditions are also more directly comparable to measurements made during experiments, which often take place below 100 GPa due to experimental difficulties above a megabar (e.g., Hirose et al., 2019; Oka et al., 2022; Tagawa et al., 2021). To our knowledge, our work is the first to study how hydrogen concentration, pressure, and temperature all combine to affect the physical properties of iron hydrides at pressures below 100 GPa.

## 2. Methods

### 2.1. Simulations

We perform AIMD simulations using the Vienna Ab initio Simulation Package (Kresse & Furthmüller, 1996) with the projector-augmented wave function method (Blöchl, 1994) and we use the Universal Molecular Dynamics package for post-processing (Caracas et al., 2021). For the exchange-correlation energy of the valence electrons, we use the Perdew-Burke-Ernzerhof form of the generalized gradient approximation (Perdew et al., 1996). The kinetic energy cutoff of the planewaves was 600 eV. Iron's valence electrons were $3d^7 4s^1$ and hydrogen's, $1s^1$, while iron and hydrogen's inert cores had radii of 2.3 and 1.1 Bohr, respectively (Figure S1 in Supporting Information S1). The simulations were within the canonical ensemble, where the number of atoms and the volume are fixed, and the temperature is controlled with a Nosé-Hoover thermostat (Hoover, 1985; Nosé, 1984). We sample the Brillouin zone at the Gamma point. We use a timestep of 0.5 fs to account for the high diffusivity of hydrogen. The first 1,000 timesteps were discarded in each simulation to ensure that the melts were well thermalized.

We simulate non-spin polarized iron hydrides with the atomic assemblages $Fe_{108}H_{12}$ ($Fe_{0.9}H_{0.1}$, $X = 0.1$), $Fe_{108}H_{54}$ ($Fe_{0.67}H_{0.33}$, $X = 0.33$), $Fe_{108}H_{108}$ ($Fe_{0.5}H_{0.5}$, $X = 0.5$) and $Fe_{108}H_{162}$ ($Fe_{0.4}H_{0.6}$, $X = 0.6$). Each composition was simulated at 3,000, 4,000, and 5000 K at a low density corresponding to approximately 10 (9–12) GPa and at a high density corresponding to 100 (98–102) GPa for 18–25 ps in order to characterize bonding, diffusivity, and viscosity in the melts (Figure 1).

In addition, we perform 1–5 ps nonspin polarized simulations at approximately 35 (33–37), 50 (50–54), and 75 (75–77) GPa at each temperature for each iron hydride to provide additional points to fit our equation of state (EOS). Magnetism increases the effective size of the atomic core; therefore, if there is magnetism, pressures in spin-polarized systems, $P_{SP}$, can be elevated relative to pressures in nonspin - polarized systems, $P_{NSP}$, of the same density. To quantify the effect of iron's magnetism in the EOS, we simulated pure iron for ≥2 ps at six volumes from 0 to 115 GPa and 3,000 K in both spin-polarized and non-spin-polarized states. Further, we simulated each iron hydride composition ($X = 0.1$, 0.33, 0.5, and 0.6) at 3,000, 4,000, and 5000 K at a volume corresponding to approximately $P_{NSP} = 1$ (0–1.7) GPa in both spin-polarized and non-spin polarized states for 0.5–1 ps. By doing so, we are able to quantify the effect of magnetism on the iron hydride EOS (specifically, $\Delta P = P_{SP} - P_{NSP}$ as a function of temperature and composition) without the computational expense of running every simulation spin-polarized, which can be up to an order of magnitude slower than non-spin polarized simulations (Figures S2 and S3 in Supporting Information S1).

### 2.2. Melt Structure

To describe the bonding environment around each type of atom, we compute the radial pair distribution function, or $g_{A-B}(r)$. The $g_{A-B}(r)$ is obtained by averaging the interatomic distance between the central atom ($A$) and the ligand atom ($B$) over time and for every A–B pair renormalized by the atomic density. The typical $g_{A-B}(r)$ is zero below the distance where the electronic repulsion is too strong to accommodate neighboring atoms. With increasing $r$, this exclusion zone is followed by an increase up to a first maximum, which defines the most

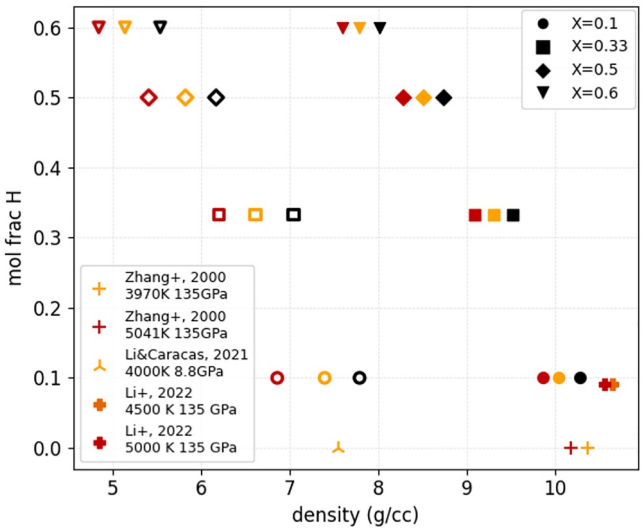


**Figure 1.** Mole fraction of hydrogen in the melts as a function of mass density, where color represents temperature (black: 3,000 K, gold: 4,000 K, scarlet: 5,000 K) and shape represents composition as referred to in the legend. Each composition was simulated at two densities at each temperature, the lower corresponding to approximately a non-spin polarized pressure, $P_{NSP}$, of 10 GPa (hollow symbols) and the higher to a $P_{NSP}$ of 100 GPa (solid symbols). The mass density of the melts increases with pressure, decreases with temperature, and decreases with hydrogen concentration. Plotted for comparison are densities of pure iron (thin crosses: Zhang et al., 2000, triangle cross: Li & Caracas, 2021) and $Fe_{0.91}H_{0.09}$ (thick crosses: Li et al., 2022) at similar pressures and temperatures, indicated in the legend, to this study; pure iron is denser than the iron hydrides. The density of $Fe_{0.91}H_{0.09}$ from Li et al. is higher than $Fe_{0.9}H_{0.1}$ from this study as there is a 35 GPa difference.

common bond length between the two atomic types. The $g_{A-B}(r)$ then drops until it reaches a first minimum, which defines the radius of the first coordination sphere of atom $A$ by atom $B$. The pattern of maxima and minima repeats for subsequent coordination spheres, eventually converging to $g_{A-B}(r) = 1$ at large interatomic distance.

The average A–B coordination number is the average number of atoms of type $B$ bonded to an atom of type $A$; it is found as the integral of the $g_{A-B}(r)$ up to the radius of the first coordination sphere. Since this represents an average over all local configurations during the time of the simulation, the coordination numbers may be fractional.

We further use the $g_{A-B}(r)$ to perform a chemical speciation analysis of the melts. Bonding is understood geometrically, where if two atoms are at a distance smaller than the first coordination sphere, they are considered to be bonded at this timestep. This is not necessarily true electronic bonding but only a measure of proximity as a function of time. Thus, atoms form a connectivity network, and various atomic clusters can be identified and tracked over time.

### 2.3. Equation of State

To fit our pressure, volume, temperature, and composition ($PVT$-$X$) EOS, we use data from this study on Fe, $Fe_{0.9}H_{0.1}$, $Fe_{0.67}H_{0.33}$, $Fe_{0.5}H_{0.5}$, and $Fe_{0.4}H_{0.6}$ with pressures corrected to account for magnetism.

The isothermal pressure-volume relation at the reference temperature, $P_{\mathrm{Tref}}(V)$, is described using either the Birch-Murnaghan or the Vinet EOS, containing fitted parameters for reference state volume, $V_0$, bulk modulus, $K_0$, and the pressure derivative of bulk modulus, $K_0$'. The thermal pressure, $\Delta P_{th}(V, T)$, is based on the Mie-Grüneisen EOS, $P(V, T) = P_{\mathrm{Tref}}(V) + \Delta P_{th}(V, T)$:

$$\Delta P_{th}(V,T) = (\gamma/V)\left(E_{th}(V,T) - E_{th}(V,T_{ref})\right)$$

where the Grüneisen parameter is $\gamma = \gamma_0(V/V_0)^q$ and $q$ is fixed to 1. The reference temperature, $T_{\mathrm{ref}}$, is 4,000 K, the median temperature in our study. The thermal energy is as described by Ichikawa et al. (2014) for metallic melts:

$$E_{th}(V,T) = 3\mathrm{NR}\left(T + e_0(V/V_0)^g T^2\right)$$

where $N = 1$ for the melts and $R$ is the gas constant. The first term describes the phonon contribution at the harmonic high temperature limit, while the second term describes the electronic and anharmonic contributions to the thermal energy. We fix $e_0$ to the values fit by Ichikawa et al. of pure iron ($e_0 = 0.314 \times 10^{-4}\ \mathrm{K}^{-1}$) and fit only $g$ to avoid the strong trade-offs and resulting overparameterization that result from fitting both $e_0$ and $g$.

We employ linear fits to capture the compositional dependence of the volume, bulk modulus, and Grüneisen parameter:

$$V_0 = V_{0\,X=0} + V_1 X$$

$$K_0 = K_{0\,X=0} + K_1 X$$

$$\gamma_0 = \gamma_{0\,X=0} + g_1 X$$

where $X$ is the mole fraction of hydrogen. The resulting $PVT$-$X$ EOS has fitted values for $V_{0\,X=0}$, $K_{0\,X=0}$, $K_0$', $\gamma_{0\,X=0}$, $g$, $V_1$, $K_1$, and $g_1$ (Table 1).

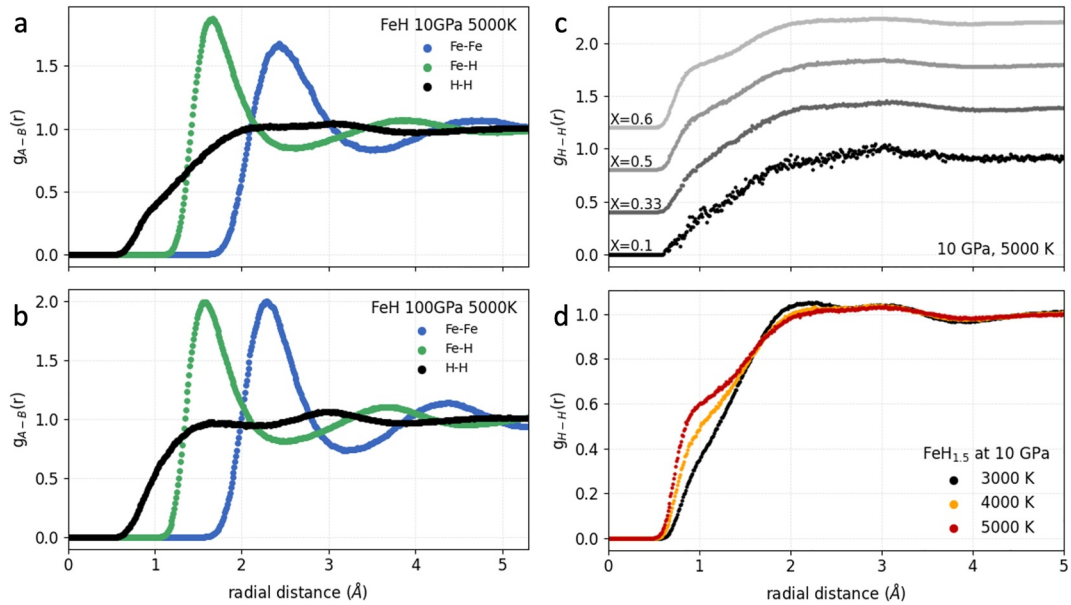


**Figure 2.** Typical pair distribution functions ($g_{A-B}(r)$) of the bonds in the iron hydride melts, shown at 5,000 K and $P_{NSP}$ = 10 GPa (a) and 100 GPa (b) for $Fe_{0.5}H_{0.5}$. The $g_{Fe-Fe}(r)$ and $g_{Fe-H}(r)$ follow a structure typical of melts with a pronounced first peak and trough. By contrast, the $g_{H-H}(r)$ is flat with values around 1: the probability of finding a hydrogen a certain distance from another is approximately equal. At 100 GPa, the $g_{H-H}(r)$ increases more quickly to $g_{H-H}(r) = 1$; hydrogen is more likely to be further from itself at low pressure. The 10 GPa $g_{H-H}(r)$ at 5,000 K for each composition lifted from the $y$-axis for ease of comparison (c). A peak at around 1 Å develops as the hydrogen concentration increases, indicating increased amounts of molecular hydrogen. The $g_{H-H}(r)$ in $Fe_{0.4}H_{0.6}$ at 3,000, 4,000, and 5,000 K (d). The molecular peak gains strength as temperature increases.

### 2.4. Transport Properties

We confirm the diffusive behavior of the atoms based on their mean-squared displacements (MSD), where the MSD is a measurement of the average distance traveled by an atom over time. In a liquid within the diffusive regime, the MSD will increase linearly with time. To calculate the self-diffusion coefficients in the melt, we use the Einstein-Stokes relation, connecting the diffusivity to the slope of the average MSD of each atomic type.

We calculate the shear viscosity of the melts using the Green-Kubo formula, which utilizes the time integral of the autocorrelation of the shear components of the stress tensor, $\sigma_{ij}$ ($i \neq j$), over time:

$$\eta = \frac{V}{k_B T} \sum_{i,j} \int_0^{\infty} \langle \sigma_{ij}(t+\tau)\sigma_{ij}(t) \rangle \, \mathrm{dt}$$

Where $V$ is the volume of the simulation cell, $k_B$ is the Boltzmann constant, $T$ is temperature, $t$ is simulation time, and the time window between sampling the correlation is $\tau$. The autocorrelations of the stresses are calculated using a $\tau$ = 2,000 fs time window. The first instance where the mean autocorrelation function (averaged over $\sigma_{XY}$, $\sigma_{XZ}$, and $\sigma_{YZ}$) crosses zero is where we determine the viscosity of the melt (as in Zhang et al., 2000). The error of the viscosity represents the standard deviation between viscosity given by the time autocorrelation of the individual shear stresses, $\sigma_{XY}$, $\sigma_{XZ}$, and $\sigma_{YZ}$.

## 3. Results and Discussion

### 3.1. Average Coordination of Iron

The $g_{Fe-Fe}(r)$ and $g_{Fe-H}(r)$ of the iron hydrides have a structure typical of melts (Figures 2a and 2b). The average coordination numbers (CN) of iron reflect how the bonding environment of iron is affected by pressure, temperature, and hydrogen concentration.

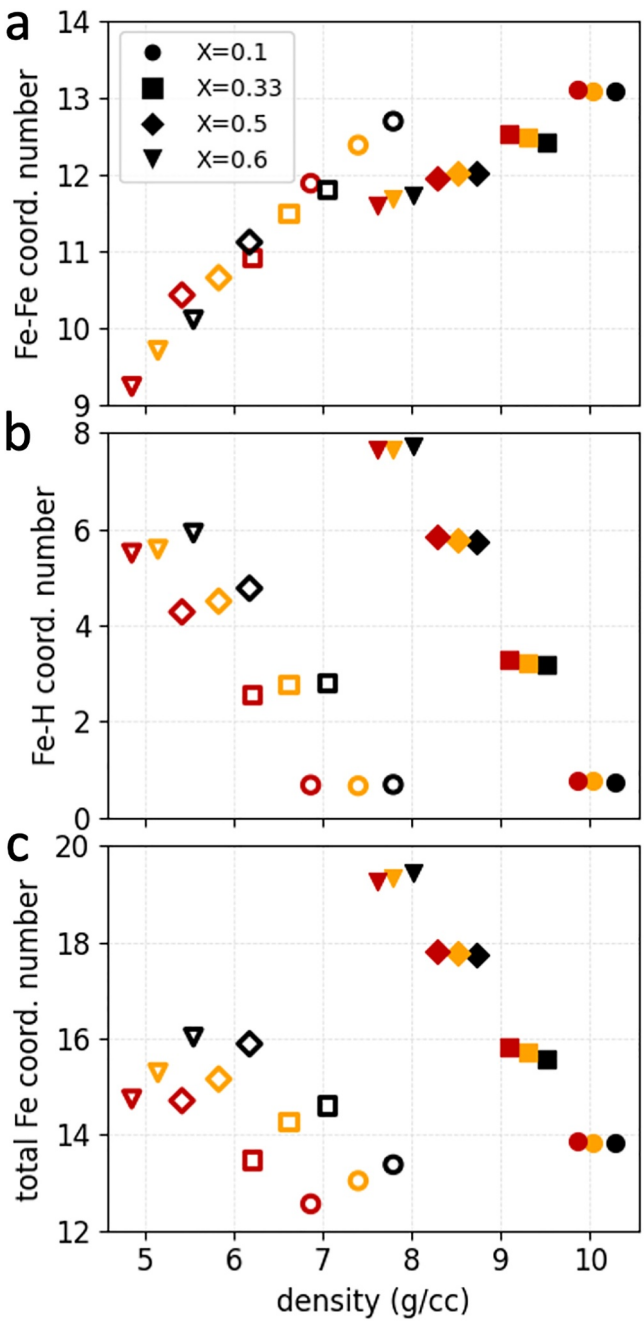


**Figure 3.** Average Fe–Fe (a), Fe–H (b), and total iron (c) coordination numbers in the $P_{NSP}$ = 10 (hollow symbols) and 100 GPa (filled symbols) melts as a function of density (black: 3,000 K, gold: 4,000 K, scarlet: 5,000 K). $CN_{Fe–Fe}$ falls from above close packed (CN = 12–13) to below close packed (as low as CN = 9) as hydrogen concentration increases. $CN_{Fe–Fe}$ decreases more rapidly in the 10 GPa melts compared to 100 GPa: in $Fe_{0.4}H_{0.6}$, the $CN_{Fe–Fe}$ is ∼9.7 at 10 and ∼11.7 at 100 GPa. $CN_{Fe–H}$ increases, naturally, as more hydrogen is available in the melt, such that despite the fall in $CN_{Fe–Fe}$, $CN_{total\ Fe}$ increases as a function of hydrogen concentration. $CN_{total\ Fe}$ is always higher at 100 GPa than at 10 GPa for the same composition, pressure, and temperature.

The average Fe–Fe coordination increases with density and decreases with hydrogen concentration (Figure 3a). Hotter melts clearly have lower coordination numbers at 10 GPa, while there is little temperature dependence at 100 GPa. Solid iron would be close-packed ($CN_{Fe–Fe}$ = 12) at the high pressures and temperature of our study. It has been previously observed that pure liquid iron at 132 GPa and 4,300 K has a coordination number of 13.2 due to the even higher packing efficiency in the liquid state (Alfè et al., 2000). At 10 GPa, $CN_{Fe–Fe}$ decays from 12.3 in $Fe_{0.9}H_{0.1}$ to 9.7 in $Fe_{0.4}H_{0.6}$, well below close-packed, and hotter melts clearly have lower coordination numbers. At 100 GPa, $CN_{Fe–Fe}$ is 13.08 in $Fe_{0.9}H_{0.1}$, above close-packed, like pure liquid iron at megabar pressures, and it falls to 11.7 in $Fe_{0.4}H_{0.6}$, slightly below close-packed.

$CN_{Fe–H}$ increases as more hydrogen is available for the iron to bond to, from only 0.72 in $Fe_{0.9}H_{0.1}$ to 6.7 in $Fe_{0.4}H_{0.6}$ (averaged for all temperatures and both pressures) (Figure 3b). Overall, while the $CN_{Fe–Fe}$ falls with hydrogen content, the increase in $CN_{Fe–H}$ results in an increase in the total CN of iron (Figure 3c). This is a clear indication that hydrogen is interstitial to the molten iron rather than substituting for iron in the coordination environment. Hydrogen substitution for iron would result in the total iron coordination number remaining ∼12 (Ohmura et al., 2020). Between $X$ = 0.1 and 0.6 at 10 GPa, the average iron atom gains within its first coordination sphere 1.9 atoms of hydrogen for each iron it loses. At 100 GPa, the H–Fe tradeoff in iron coordination is more extreme because atoms are more tightly bound: the average iron atom gains 4.9 atoms of hydrogen for each iron it loses.

The temperature dependence of the coordination is more pronounced at 10 versus 100 GPa. This is due to the fact that hotter melts will have more volume contrast with colder melts at low pressures than at high pressures (i.e., thermal expansivity is higher at low pressure), and thus average coordination numbers have a more obvious decrease with increasing temperature in the lower-pressure melts.

### 3.2. Iron-Iron and Iron-Hydrogen Bond Distances

The Fe–Fe and Fe–H interatomic bond distances are defined by the positions of the first peak of the $g_{Fe–Fe}(r)$ and $g_{Fe–H}(r)$, respectively (Figures 4a and 4b). Fe–Fe bond distance decreases with increasing temperature, consistent with X-ray diffraction experiments and molecular dynamics simulations observing negative expansion in a series of metallic melts (Lou et al., 2013). At the same temperature and composition, the 100 GPa bond length is shorter than 10 GPa as compaction shortens the bonds. The average length of an Fe–Fe bond increases with hydrogen concentration: at 10 GPa, it increases from 2.36 Å to 2.47 Å (averaged for the three temperatures) between $X$ = 0.1 and 0.6. At 100 GPa, the rate of change is very similar while the bond lengths are shorter due to the higher compression, increasing from 2.23 Å to 2.34 Å between $X$ = 0.1 and 0.6 (Figure 4a). The molar volume decreases as a function of hydrogen concentration (see the EOS), and the increase in Fe–Fe bond length and the decrease in the $CN_{Fe–Fe}$ is reflective of this trend: hydrogen atoms replace iron in the unit, so the average distance between iron atoms grows.

The Fe–H bond distance becomes slightly shorter as the hydrogen concentration increases at 10 GPa, falling from 1.68 Å to 1.63 Å between $X$ = 0.1 and 0.6. At 100 GPa, the change in the Fe–H bond length with composition becomes negligible, as the bond length is very similar at the same temperature regardless of composition (Figure 4b).

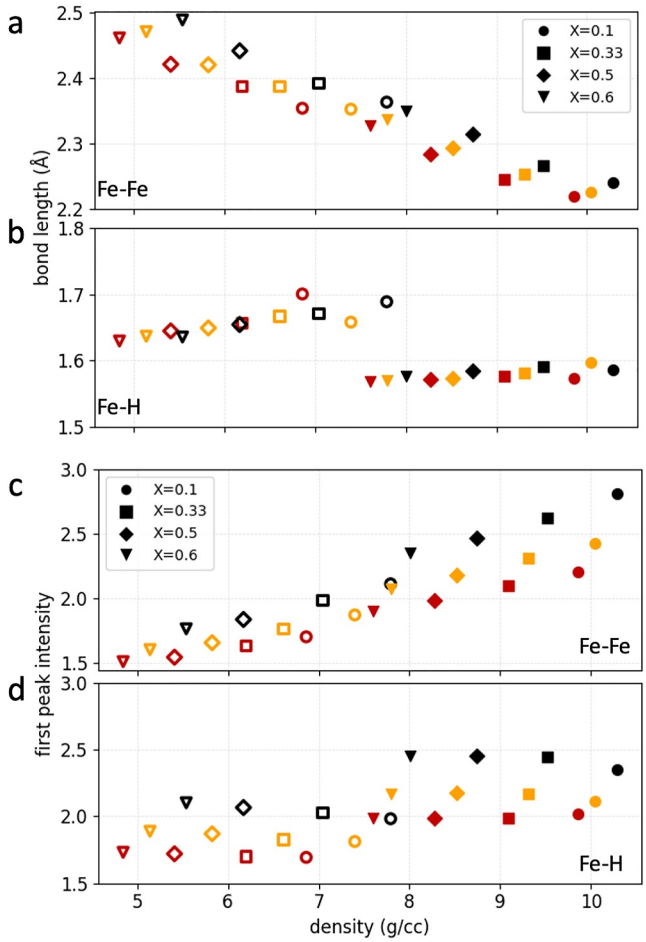


**Figure 4.** Fe–Fe (a) and Fe–H (b) bond length in the melts as a function of density (black: 3,000 K, gold: 4,000 K, scarlet: 5,000 K) in the $P_{NSP} = 10$ (hollow symbols) and 100 GPa (filled symbols). The variation in bond length is small, within 0.3 Å. Bonds are closer at higher temperature and higher pressure. Fe–Fe bonds become shorter as density increases. The more hydrogen-rich the composition, the longer the Fe–Fe bond. The Fe–H bond length varies little, negligibly so at 100 GPa. At 10 GPa, Fe–H bonds are slightly closer in more hydrogen-rich melts. Intensity of the first peak in Fe–Fe (c) and Fe–H (d) $g_{A-B}(r)$. In general, higher temperature, lower pressure, and lower density (more hydrogen-rich) result in broader peaks. The Fe–Fe peak intensity decays as hydrogen is added, as hydrogen causes the peak to broaden (meaning a larger variety of Fe–Fe bond lengths). The Fe–H peak is slightly sharper in more hydrogen-rich melts compared to less hydrogen-rich melts at the same temperature and pressure.

The intensity of the first peak in the $g_{A-B}(r)$ gauges the sharpness of the peak and thus the variety of bond lengths (Figures 4c and 4d). Hotter melts have lower intensity and thus more diffuse peaks in the $g_{A-B}(r)$. Increasing pressure sharpens the peak in a melt with a given composition and temperature. The addition of hydrogen causes the $g_{Fe-Fe}(r)$ peak to broaden: the intensity of the first peak of the $g_{Fe-Fe}(r)$ falls between $X = 0.1$ and 0.6, and the rate of change is similar between 10 and 100 GPa (Figure 4c). The intensity of the first peak of the $g_{Fe-H}(r)$ remains relatively steady with composition at a given temperature and pressure, but more hydrogen-rich melts have a slightly sharper peak in the $g_{Fe-H}(r)$, especially at 3,000 K (Figure 4d).

### 3.3. Chemical Speciation of Hydrogen

The $g_{H-H}(r)$ increases gradually to level off at $g_{H-H}(r) = 1$ without exhibiting strong peaks at any pressure or temperature. The fact that $g_{H-H}(r)$ does not exceed a value of ~1 indicates that the probability of finding a hydrogen within a certain distance from another hydrogen is similar regardless of interatomic distance (Figures 2c and 2d). This indicates that the hydrogen is mostly atomic and is distributed throughout the melt without a bonding preference to itself (Li et al., 2022; Ohmura et al., 2020; Posner & Steinle-Neumann, 2019). However, a shoulder in the 10 GPa $g_{H-H}(r)$ develops around 1 Å starting in $Fe_{0.5}H_{0.5}$. The likelihood of a pair of hydrogen atoms being in proximity below an interatomic distance of ~1 Å steadily increases from $X = 0.1$ to $X = 0.6$ (Figure 2c). This represents an increasing amount of molecular hydrogen, which has a bond distance of about 1 Å in liquid form (Zong et al., 2020). The shoulder grows in strength as temperature increases (Figure 2d).

To track the behavior of molecular hydrogen, we use a speciation analysis of the $H_{x \geq 1}Fe_{y \geq 0}$ chemical species (Figure 5). We use a constant, molecular H–H bond length (1.23 Å), while Fe–Fe and Fe–H bond lengths are fit for each melt from the $g_{A-B}(r)$ of that melt. A cluster is defined when an iron or a hydrogen is within the H–Fe or H–H coordination sphere, respectively.

The abundance of species with more than one hydrogen increases with (a) temperature, (b) pressure, as the atoms are pushed together and thus form larger clusters, and (c) as the hydrogen concentration increases. Between $Fe_{0.9}H_{0.1}$ and $Fe_{0.4}H_{0.6}$, the proportion of $H_{x>1}Fe_{y\geq0}$ clusters increases from 0.5 (0.9)% to 9.7 (14.4)% at 10 GPa at 3,000 K (5,000 K) and from 0.6 (1.4)% to 14.8 (21.3)% at 100 GPa and 3,000 K (5,000 K). Chemical species break and form rapidly in the melts due to the high diffusivities, and the $H_2$ molecules in each melt have average lifetimes of 6 fs or less.

As hydrogen concentration increases, both atomic and molecular hydrogen clusters become less iron rich (and more hydrogen rich) because the hydrogen to iron ratio increases. For example, the most abundant species in $Fe_{0.9}H_{0.1}$ is $H_1Fe_6$ at 10 GPa (33% of all species at 5,000 K) and $H_1Fe_7$ at 100 GPa (25% of all species at 5,000 K) (Figures 5a and 5c). In $Fe_{0.4}H_{0.6}$, the most abundant species are $H_1Fe_4$ at 10 GPa (29% of all species at 5,000 K) and $H_1Fe_5$ at 100 GPa (30% of all species at 5,000 K) (Figures 5b and 5d). Molecular hydrogen clusters ($H_{\geq2}Fe_{y \geq 0}$) have on average more iron than atomic clusters: $H_2$ clusters have 0.55 more iron atoms than $H_1$ clusters at 10 GPa, and 0.9 more iron atoms at 100 GPa.

Pure hydrogen molecules, that is, $H_{\geq2}$ without any iron in either hydrogen's coordination sphere, are very rare. Pure $H_{\geq2}$ is most abundant in $Fe_{0.4}H_{0.6}$ at 10 GPa and 5,000 K, making up only 0.016% of all species; it does not exist at all at 100 GPa nor in $Fe_{0.9}H_{0.1}$ or $Fe_{0.67}H_{0.33}$ at 10 GPa. Thus, even though there is a significant amount of molecular hydrogen in the melts, the molecules remain dissolved within the iron, occupying interstitial sites rather than exsolving.

**Table 1**
*Fitted Parameters of the PVT-X Equation of State (EOS)*

| | Fitted value | Std. Error |
|---|---|---|
| $V_{0\ X=0}$ | 8.69 | 0.08 |
| $K_{0\ X=0}$ | 55.9 | 4.6 |
| $K_0'$ | 5.54 | 0.19 |
| $\gamma_{0\ X=0}$ | 1.44 | 0.07 |
| $g$ | −4.00 | 0.17 |
| $V_1$ | −4.83 | 0.09 |
| $K_1$ | −55.0 | 4.5 |
| $g_1$ | −1.39 | 0.10 |

*Note.* Standard statistical error is $\pm 1\sigma$. Units are $cm^3$/mol for volume and GPa for bulk modulus. For this fit, the reference temperature is 4000 K and the Birch-Murnaghan EOS is used.

### 3.4. Equation of State

We develop a *PVT-X* EOS for the iron hydride melts to describe the relationships of these physical parameters (Table 1). We apply a pressure correction based on the effects of the magnetism of iron before fitting the EOS, such that $P = P_{NSP} + \Delta P$. We find that in pure iron at 3,000 K, the pressure difference between the spin-polarized and non-spin polarized systems at the same volume, $\Delta P = P_{SP} - P_{NSP}$, falls linearly as a function of $P_{NSP}$ as the magnetization of iron diminishes. At $P_{NSP} = 0$ GPa, $\Delta P$ is 9.9 GPa and $\Delta P$ goes to zero around 115 GPa (Figure S2 in Supporting Information S1). In the iron hydrides, there is a reduction in the magnetization of iron (i.e., smaller $\Delta P$) with increasing temperature and increasing hydrogen concentration. Due to the high computational expense of the spin-polarized simulations, we assume that, like in iron at 3,000 K, the pressure difference for each composition at each temperature decreases linearly and becomes zero at 115 GPa. Based on this assumption, $\Delta P$ at $P_{NSP} = 0$ GPa ranges from 7.6 GPa in $Fe_{0.9}H_{0.1}$ at 3,000 K to 1.6 GPa in $Fe_{0.4}H_{0.6}$ at 5,000 K (Figure S3 in Supporting Information S1).

The $V_0$ of the melts decreases from 8.7 $cm^3$/mol in iron to 5.8 $cm^3$/mol in $Fe_{0.4}H_{0.6}$ (Figure 6a), as hydrogen replaces iron in the formula unit $Fe_{1-X}H_X$ and the mass density falls (Ohmura et al., 2020). The melts become more compressible ($K_0$ decreases) as a function of hydrogen concentration, from 56 GPa in iron to 22.9 GPa in $Fe_{0.4}H_{0.6}$ (Figure 6b). Because of the expansion of the iron by the uniformly distributed interstitial hydrogen in the melt, we expect hydrogen to reduce the bulk modulus relative to its dry iron counterpart (Umemoto & Hirose, 2015). The Grüneisen parameter shows a negative trend with hydrogen concentration, decreasing from 1.44 in iron to 0.59 in $Fe_{0.4}H_{0.6}$ (Figure 6c). The thermal expansivity $\alpha_0 = (\gamma_0 C_v)/(K_0 V_0)$ increases linearly with

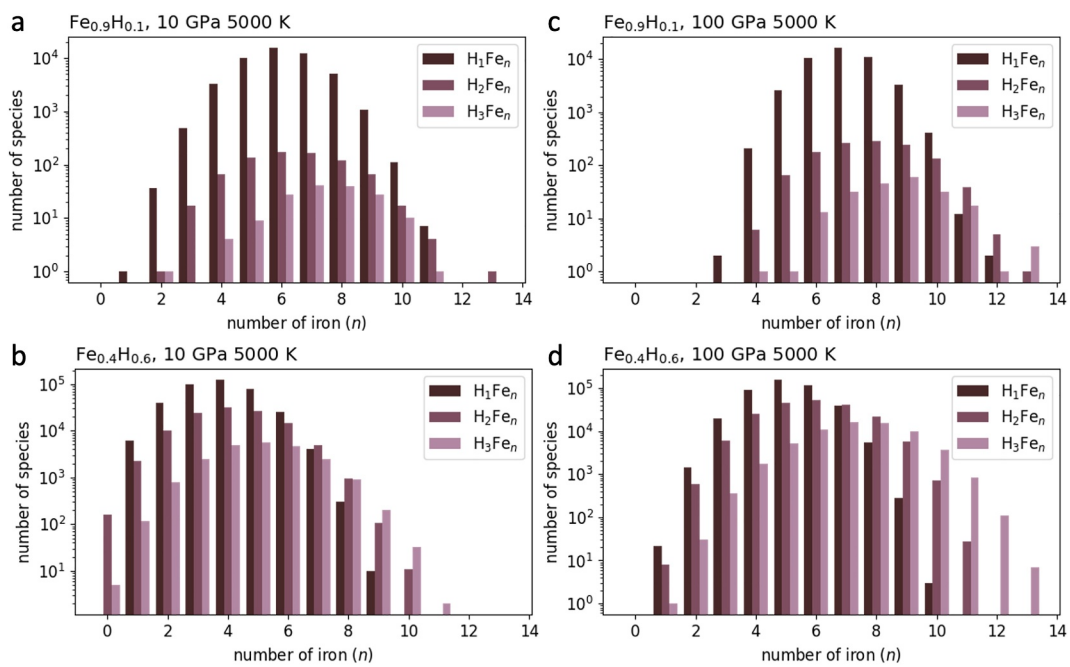


**Figure 5.** Histograms showing the number of iron within $H_1$, $H_2$, and $H_3$ clusters in $Fe_{0.9}H_{0.1}$ at 5,000 K and 10 GPa (a) and 100 GPa (c) and in $Fe_{0.4}H_{0.6}$ at 5,000 K and 10 GPa (b) and 100 GPa (d). $H_1$ clusters are dominant (note the log scale on the *y*-axis): $H_{>1}$ clusters are only 0.9% and 1.4% of all species in (a, c), and 14% and 21% in (b, d). As the hydrogen concentration increases between $Fe_{0.9}H_{0.1}$ and $Fe_{0.4}H_{0.6}$, the number of iron per $H_{1-3}$ decreases because there are more hydrogen atoms to share the same number of iron atoms. At 10 GPa, the average cluster compositions for each number of hydrogen are $H_1Fe_{4.5}$, $H_2Fe_{6.5}$, and $H_3Fe_{7.4}$ in $Fe_{0.9}H_{0.1}$ and $H_1Fe_{3.9}$, $H_2Fe_{4.2}$, and $H_3Fe_{5.0}$ in $Fe_{0.4}H_{0.6}$. At 100 GPa, the average cluster compositions are $H_1Fe_7$, $H_2Fe_{7.8}$, and $H_3Fe_{8.6}$ in $Fe_{0.9}H_{0.1}$ and $H_1Fe_{4.5}$, $H_2Fe_{5.9}$, and $H_3Fe_{7.3}$ in $Fe_{0.4}H_{0.6}$.

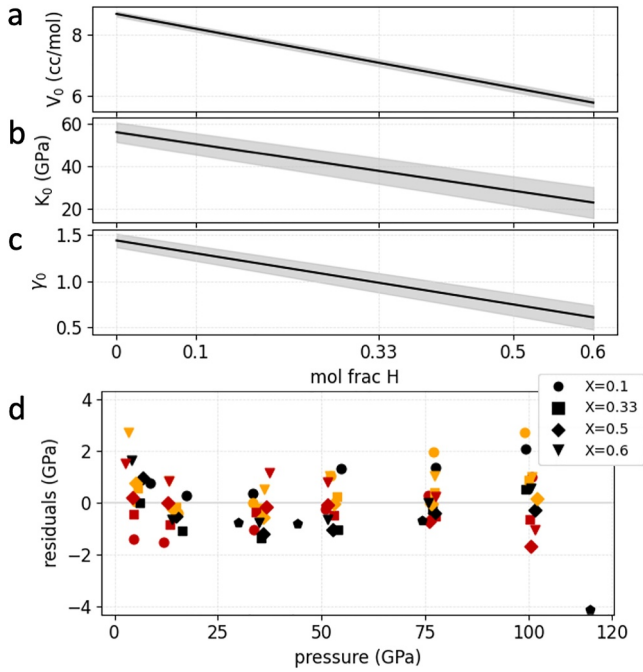


**Figure 6.** Linearly compositionally dependent physical parameters in the EOS as a function of the mole fraction of hydrogen (a–c). Gray intervals are $1\sigma$ error. $V_0$ decreases as hydrogen replaces iron in the compound $Fe_{1-X}H_X$. Since hydrogen occupies the interstices of the iron melt, the addition of hydrogen enhances compressibility: $K_0$ decreases. As hydrogen concentration increases, $\gamma_0$ decreases. Residuals of the EOS (d) are shown as a function of pressure; the residuals have an R.M.S. of 1 GPa.

hydrogen concentration as well, from $9.3 \times 10^{-5}$ $K^{-1}$ in iron to $1.4 \times 10^{-4}$ $K^{-1}$ in $Fe_{0.4}H_{0.6}$. The residuals of the EOS are almost all within 2 GPa and the R.M.S. value of the residuals is 1 GPa (Figure 6d).

This parameterization enables the calculation of equations of state in *PVT-X* space for iron hydrides up to 0.6 mol fraction hydrogen near 1–100 GPa and 3,000–5,000 K (Figure 7). Our proposed EOS can be used to estimate the properties of the cores of Moon-sized bodies (central pressure ~5 GPa) and planetary embryo-sized objects such as Mars (central pressure ~39 GPa), and with cautious extrapolation, of Venus sized bodies (core-mantle boundary pressure ~115 GPa) as well as Earth's outer core.

### 3.5. Diffusivity and Viscosity

The hotter the melt is, the higher the diffusivity of the atoms. For a melt of a given composition and temperature, diffusivities in the 100 GPa melts are lower than those at 10 GPa, as the atoms are more confined. Hydrogen is 7–14 times more diffusive than iron in the same melt. The diffusivity of iron, $D_{Fe}$, is between $10^{-9}$ and $10^{-8}$ $m^2/s$ and $D_H$ is between $10^{-8}$ and $10^{-7}$ $m^2/s$. We compare the diffusivities in our melts to those of pure iron (8.8 GPa from Li & Caracas, 2021; 135 GPa from Zhang et al., 2000) and of $Fe_{0.91}H_{0.09}$ (Li et al., 2022) at similar conditions to our work (Figure 8). As observed in an earlier work (Umemoto & Hirose, 2015), the diffusivity of both iron and hydrogen tends to increase as the melts become more hydrogen-rich: hydrogen lubricates the alloy (Figure 8). Therefore, the diffusivity of pure iron at similar pressures and temperatures is lower than that of iron hydrides. The diffusivities of iron and hydrogen in $Fe_{0.91}H_{0.09}$ at 135 GPa from Li et al., 2022 are similar but lower than $Fe_{0.9}H_{0.1}$ at 100 GPa from this study due to the higher pressure in Li et al. We find that, at 100 GPa and 3,000 K, $Fe_{0.9}H_{0.1}$ and $Fe_{0.67}H_{0.33}$ have flat MSD and thus very low diffusion, indicative of glassiness (i.e., near- or sub-liquidus conditions). Therefore, the simulations at these *PTX* conditions are excluded in the analysis of transport properties.

Posner and Steinle-Neumann (2019) found that in a dilute solution, $Fe_{0.96}H_{0.04}$, $D_{Fe}$ is actually modestly reduced. They attribute this to the fact that the iron-iron packing in $Fe_{0.96}H_{0.04}$ is unaffected relative to pure iron and thus the interstitial hydrogen block diffusion. This contrasts with our result and that of Umemoto and Hirose (2015), which are much more hydrogen-rich, with lower iron-iron coordination numbers and thus more pathways for iron diffusion (Figure 3).

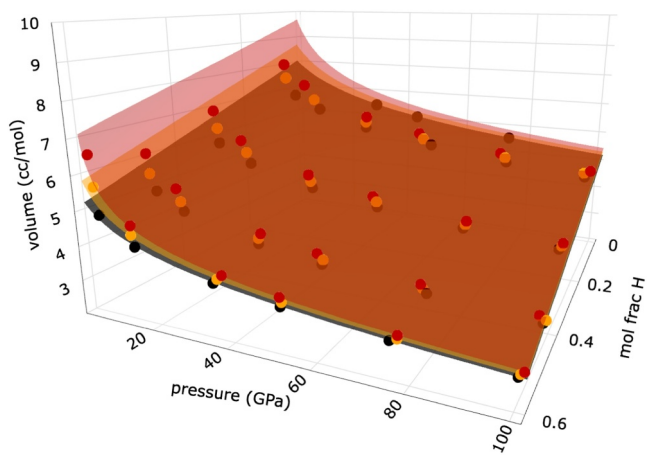


**Figure 7.** *PVT-X* isothermal surfaces from the equation of state are shown from 1 bar to 100 GPa (black: 3,000 K, gold: 4,000 K, scarlet: 5,000 K). Note the compositionally dependent physical parameters that are clearly reflected, as the volume is smaller, the melts are compacted more quickly, and the thermal expansion is more pronounced as hydrogen concentration increases.

Based on the Arrhenius law equation provided by Umemoto and Hirose (2015), we compare the diffusivities in our iron hydride melts and theirs' at 100 GPa (Figure S4 in Supporting Information S1). The trend in $D_H$ as a function of hydrogen concentration matches very well between our studies, while our $D_{Fe}$ trends slightly high. As the lowest pressures simulated by Umemoto and Hirose (2015) were 112 GPa at 4,000 K and 125 GPa at 5,000 K, and they had 76–100 iron atoms to our 108 iron atoms in each composition, we attribute the subtle differences in $D_{Fe}$ to a combination of extrapolation and size-based effects.

Hydrogen concentration has a stronger effect on the diffusivity of iron than on that of hydrogen, evidenced by the rate of change of the diffusivity with increasing density (decreasing hydrogen concentration), $d\log D/d\rho$, being more negative for iron than for hydrogen. At 10 GPa, $d\log D_H/d\rho = -0.16$ $m^2/s/g/cc$ and $d\log D_{Fe}/d\rho = -0.19$ $m^2/s/g/cc$ (averaged for all temperatures). With increasing pressure, $d\log D/d\rho$ becomes more gradual for both iron and hydrogen: at 100 GPa, $d\log D_H/d\rho = -0.06$ $m^2/s/g/cc$ and $d\log D_{Fe}/$

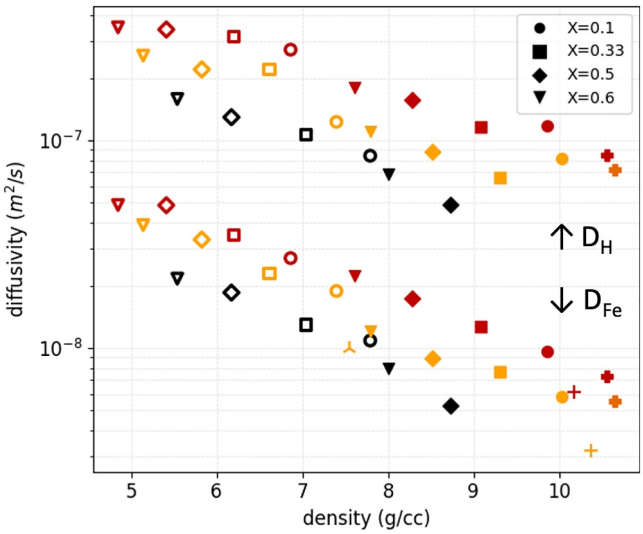


**Figure 8.** The diffusivities of iron and hydrogen in the $P_{NSP}$ = 10 (hollow symbols) and 100 GPa (filled symbols) melts as a function of density (black: 3,000 K, gold: 4,000 K, scarlet: 5,000 K). Also shown is the diffusivity of pure iron from Zhang et al. (2000) (thin crosses) and Li and Caracas (2021) (triangle cross) and of hydrogen and iron in $Fe_{0.91}H_{0.09}$ from Li et al. (2022) (thick crosses). Pressure suppresses diffusion, while temperature enhances it. Hydrogen is more diffusive than iron. As the melts become more hydrogen-rich (density decreases), the diffusivity of both iron and hydrogen generally increases. The diffusivity of the iron changes at a faster rate with density than that of hydrogen: the diffusivity of iron is more sensitive to hydrogen concentration.

$d\rho$ = −0.13 $m^2$/s/g/cc. Between $Fe_{0.9}H_{0.1}$ and $Fe_{0.4}H_{0.6}$, averaged over all temperatures, the diffusivity of iron increases by a factor of 1.9 at 10 GPa and by a factor of 1.8 at 100 GPa. The diffusivity of hydrogen increases by a factor of 1.6 at 10 GPa and by a factor of 1.2 at 100 GPa.

The iron hydride fluids are inviscid, with shear viscosities within $10^{-3}$ Pa s; for comparison, water at standard temperature and pressure has a viscosity of $10^{-3}$ Pa s (Figure 9a). The melts are more viscous at higher pressure and lower temperature. A representative example of the results from the Green-Kubo method shows convergence to a single viscosity value of ~$1.4 \times 10^{-3}$ Pa s for $Fe_{0.5}H_{0.5}$ at 10 GPa and 5,000 K (Figures 9b and 9c). The trend of viscosity as a function of composition for the iron hydrides confirms the expectation that pure iron should be more viscous than an iron hydride, and the viscosity of $Fe_{0.91}H_{0.09}$ from Li et al., 2022 agrees generally with our data, though it is slightly more inviscid than we would predict. At 10 GPa, the viscosity at a given temperature always decreases as more hydrogen is added to the melt. At 100 GPa, viscosity is very similar between 0.1 and 0.33 mol fraction hydrogen at respective temperatures before decreasing between 0.33 and 0.6 mol fraction hydrogen. On average, the viscosity increase with density (decreasing hydrogen concentration) d$\log\eta$/d$\rho$ is slower at 100 GPa than at 10 GPa: d$\log\eta$/d$\rho$ is 0.19 Pa s/g/cc at 10 GPa and 0.14 Pa s/g/cc at 100 GPa. Between $Fe_{0.9}H_{0.1}$ and $Fe_{0.4}H_{0.6}$, averaged over all temperatures, the viscosity decreases by a factor of 0.39 at 10 GPa and by a factor of 0.55 at 100 GPa.

While the viscosity is related to a planet's liquid metallic core's convective behavior and thus its potential generation of a geodynamo, the high temperatures of the core mean that convection cells can form with relative insensitivity to the viscosity of the core fluid, as long as the viscosity is low (Buffett, 2000; Jones & Schubert, 2015). AIMD studies on the viscosity of

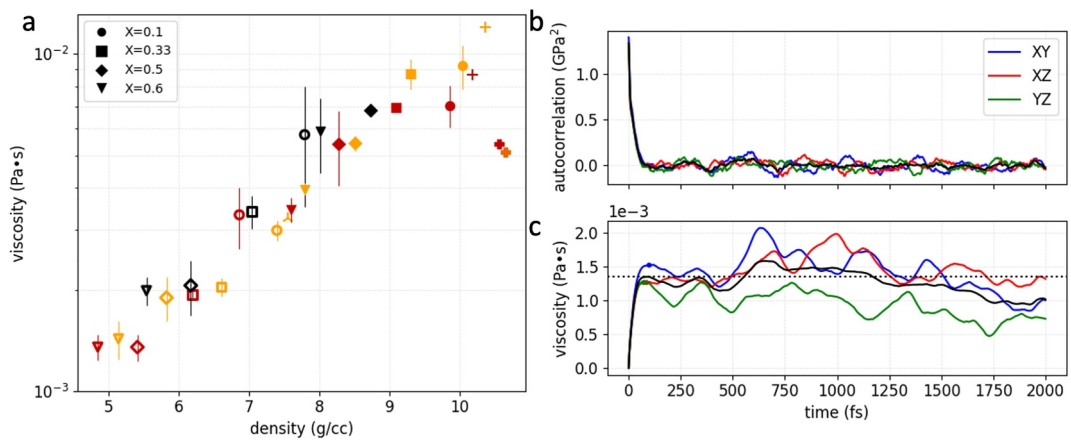


**Figure 9.** Shear viscosity of the iron hydrides (a) in the $P_{NSP}$ = 10 (hollow symbols) and 100 GPa (filled symbols) melts as a function of density (black: 3,000 K, gold: 4,000 K, scarlet: 5,000 K). The melts are less viscous at higher temperature and more viscous at higher pressure. More hydrogen-rich (less dense) melts are generally less viscous than the other melts at the same pressure and temperature. For comparison, the viscosity of pure iron from Zhang et al. (2000) (thin crosses) and Li and Caracas (2021) (triangle cross) and of $Fe_{0.91}H_{0.09}$ from Li et al. (2022) (thick crosses). Representative stress autocorrelation functions (b) and shear viscosity (c) for the shear components of the stress tensor $\sigma_{ij}$, $i \neq j$, as functions of time window for $Fe_{0.5}H_{0.5}$ at $P_{NSP}$ = 10 GPa and 5,000 K. The black curve represents the average of the results from each component of the stress tensor. The stress autocorrelation drops to zero after 100 steps. The value of the viscosity reaches convergence shortly after. The differences between shear tensor components are normal numerical effects and give a sense of the error bars in our viscosity estimates. For consistency with previous studies, we plot in (a) the viscosity values obtained when the average of the autocorrelation functions first cross zero (Zhang et al., 2000).

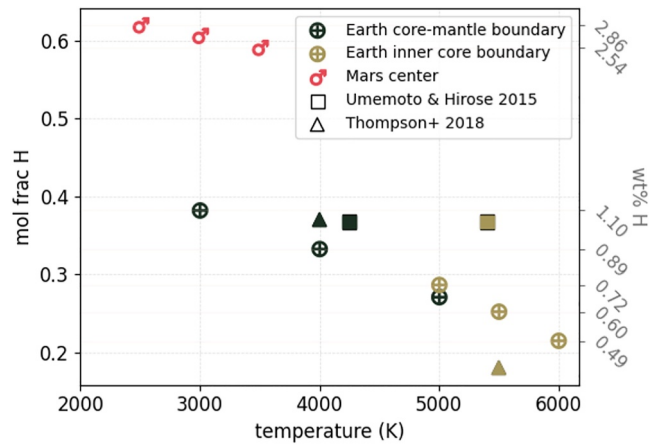


**Figure 10.** The amount of hydrogen required to reproduce the pressure and density within Earth and Mars, as a function of temperature, assuming that hydrogen is the only alloying element. Astronomic symbols denote estimates from this study; in addition, estimates from Umemoto and Hirose (2015) (squares) and Thompson et al. (2018) (triangles) are shown. Color represents pressure/density within Earth and Mars. The Martian core's low density requires 2.5–2.9 wt% hydrogen ($X = 0.59$–0.62). Earth's core requires between 0.48 and 1.1 wt% hydrogen ($X = 0.21$ to 0.38) depending on the assumed thermal gradient throughout the core. For Mars, the difference between the velocity in the seismic model and our calculated velocity ($V_{\text{diff}}$) is on average 0.22 km/s. For Earth, $V_{\text{diff}} = 0.12$ and $-0.30$ km/s at the CMB and the ICB, respectively.

iron at outer core conditions suggest that the viscosity should be quite low, around $10^{-2}$ to $10^{-3}$ Pa·s (Alfè et al., 2000; de Wijs et al., 1998; Zhang et al., 2000). As the addition of hydrogen in geochemically relevant amounts has been shown to have the strongest effect on the viscosity of liquid iron of all the light elements (Li et al., 2022; Posner & Steinle-Neumann, 2019), our work suggests that the change in iron's viscosity induced by light elements is relatively small and will not have an externally evident effect on the transport properties of the liquid cores of telluric planets.

### 3.6. Estimating Core Compositions

Using our EOS, we can estimate the hydrogen concentration that reproduces the density of the liquid cores of Earth and Mars. To estimate the seismic compressional velocity of the iron hydrides, $V_p = (K_S/\rho)^{1/2}$, the adiabatic bulk modulus, $K_S$, was calculated as $K_S = K_T + \gamma^2 C_V T/V$, where $C_V$, the constant volume heat capacity, is $(\partial E_{th}/\partial T)_V$ and $K_T$, the isothermal bulk modulus, is $-V(\partial P/\partial V)_T$. The iron hydrides that match the density and pressure determined by models of the Martian and terrestrial core do not necessarily match the sound velocities given by those models, emphasizing the fact that a binary alloy is overly simple to describe them. In general, we estimate that large concentrations of hydrogen describe the core density deficits of Earth's and Mars's cores; these are the upper bounds, and both Earth and Mars undoubtably have a mixture of light other elements, such as carbon, sulfur, silicon, and oxygen, that contribute to their density deficits and velocity difference relative to pure iron. It's noteworthy that hydrogen, being the lightest element, is required in the largest fraction of all light elements in order to account for the density deficits in the terrestrial and Martian cores on its own. Due to this and the extrapolation of the pressure conditions of this study to the conditions of Earth's outer core, the following estimates for hydrogen concentration and sound velocity based on our EOS are intended to give general ideas about the amount of hydrogen that could reproduce the densities of the cores of Mars and Earth.

The density at the center of Mars is estimated to be only ~6.538 g/cc, and is probably mostly molten (Irving et al., 2023). Assuming a central pressure of 40 GPa, we estimate maximum super-hydrous conditions: between $X = 0.62$ (2.85 weight%) and $X = 0.59$ (2.54 weight%) hydrogen at 2,500 and 3,500 K, respectively (Figure 10). These iron hydrides have slower sound velocities than observed on Mars, with a mean velocity difference between the seismic model and our calculation ($V_{\text{diff}} = V_{\text{model}} - V_{\text{calc}}$) of 0.22 km/s, assuming a sound velocity of 5.9 km/s at the center of Mars (Irving et al., 2023).

In the Earth, at the core-mantle boundary (CMB), we estimate a maximum hydrogen concentration ranging from $X = 0.38$ (1.10 weight%) at 3,000 K to $X = 0.27$ (0.66 weight%) at 5,000 K, assuming a density of 9.996 g/cc (Irving et al., 2018). The amount of hydrogen needed to reproduce the pressure and density at the ICB lies at the

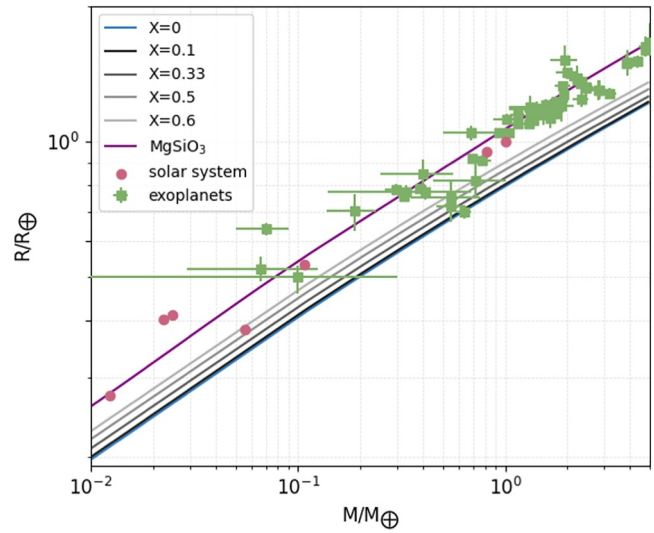


**Figure 11.** Mass-radius relationship of pure, molten iron (blue curve) and iron hydride (black-gray curves) bodies, based on our equation of state and assuming a potential temperature of 3,000 K for the adiabatic temperature profile. A cold curve for a pure $MgSiO_3$ planet is shown in purple (Seager et al., 2007; Zeng & Seager, 2008). Earth, Venus, Mars, Mercury, Ganymede, Titan, and the Moon are plotted as pink circles. The exoplanet population, plotted as green squares, was taken from the Nasa Exoplanet Archive and includes all exoplanets <2 Earth radii and <5 Earth masses and for which error in mass/radius is less than 0.3 Earth masses/radii.

lower range of the CMB estimates, from $X = 0.29$ (0.72 weight%) at 5,000 K to $X = 0.21$ (0.49 weight%) at 6,000 K, assuming a density of 12.317 g/cc (Irving et al., 2018) (Figure 10). Assuming sound velocities of 7.999 and 10.349 km/s at the CMB and ICB, respectively (Irving et al., 2018), these iron hydrides result in an average $V_{diff}$ of 0.12 km/s at the CMB and a $V_{diff}$ of −0.28 km/s at the ICB. Following a thermal gradient from 4,000 K at the CMB to 5,500 K at the ICB, the hydrogen concentration would need to decrease from 0.89 to 0.60 weight% ($X = 0.33$ to 0.25) to match the density of the outer core. Using the Vinet formalism for isothermal compression (rather than the Birch-Murnaghan) does not meaningfully change the compositional estimates. Due to the different extrapolations between the EOS, at the ICB at 5,500 K, the difference in $X$ is +0.01 and $V_{diff}$ is −0.06 km/s instead of −0.29 km/s.

Our results are within the estimates from Thompson et al. (2018), who, from the synthesis and extrapolation of high-pressure, high-temperature experimental data on pure iron and $FeH_x$ as well as on a theoretical static equations of state of solid $FeH_x$, estimate 0.8–1.3 weight% hydrogen at the CMB with $T_{CMB} = 4{,}000 \pm 500$ K and 0.2–0.6 weight% hydrogen at the ICB with $T_{ICB} = 5{,}500 \pm 500$ K, compared to PREM. Umemoto and Hirose (2015) is another AIMD study which finds ∼1 weight% hydrogen explains the density of the entire outer core given by PREM, assuming a geotherm with $T_{CMB} = \sim 4{,}250$ K and $T_{ICB} = 5{,}400$ K. Our results are similar, but estimate less hydrogen, especially at the ICB (Figure 10).

Our EOS can also aid in the interpretation of the mass-radius relationship of small exoplanets and solar system bodies (including moons) for which we lack seismic observations (Figure 11). These mass-radius relationships are commonly used to decipher the plausible compositions of planetary bodies, as proportions of rock (silicate), metal (iron-rich core), and ice. Even very hydrogen rich iron hydrides generate model planetary masses substantially greater than silicates, although the inferred rock/metal ratio can be significantly impacted by the incorporation of hydrogen into the metal portion of a planet (Figure 11).

## 4. Conclusions

In this study, we explore how the addition of hydrogen between a mole fraction of 0.1 and 0.6 changes the structure of iron hydride melts. The average Fe–Fe coordination decreases from near close-packed (11.9–13.1) in $Fe_{0.9}H_{0.1}$ to 9.2–11.7 in $Fe_{0.4}H_{0.6}$. In tandem, the average Fe–H coordination increases from less than one to 5.6–7.7. The $g_{H-H}(r)$ indicates the presence of molecular hydrogen bonds in $Fe_{0.5}H_{0.5}$ and $Fe_{0.4}H_{0.6}$ at 10 GPa. Analysis of hydrogen's speciation shows that the proportion of molecular hydrogen increases from fractions of

percent in $Fe_{0.9}H_{0.1}$ to 10%–20% in $Fe_{0.4}H_{0.6}$, and that the hydrogen molecules remain immersed in the iron melt. By fitting a *PVT-X* EOS, we quantify how increasing the hydrogen concentration causes the melts' molar volume and Grüneisen parameter to decrease and the compressibility and thermal expansivity to increase. We use our EOS to estimate the compositions of Earth's outer core and Mars's core and to help interpret mass-radius relationships in exoplanets. We observe that as the hydrogen concentration increases, both iron and hydrogen become more diffusive. Correspondingly, the melts become more inviscid.

In reality, planetary cores with as much as 60% hydrogen are likely to be extraordinary. There are obstacles to planets gaining and retaining hydrogen: in Earth and other rocky planets that form within the snowline, the fact that the accretionary material could have been mostly dry is a limiting factor; however, the in-gassing of hydrogen-rich atmospheres through magma oceans and the delivery of hydrogen-rich material during accretion are two viable ways to introduce hydrogen to the cores of planets. But hydrogen is very unlikely to be the sole alloying element in a liquid iron core. Planet-building is not a clean process, and light elements have the potential to augment others' chemical behavior within the core (e.g., Fu et al., 2023; Hirose et al., 2019). These complex chemical interactions, as well as the physical processes that develop the chemistry, will ultimately determine the core's composition (Hirose et al., 2021). Regardless, an understanding of binary Fe–X alloys helps add constraints to build ever more accurate models for iron-rich cores.

## Data Availability Statement

The EOS, diffusivity, viscosity, coordination, bond length, and speciation results presented in this study are available at Stoutenburg (2024).

**Acknowledgments**
ERS, AJC, and RC acknowledge support from the FACCTS program at Univ. of Chicago and from the CNRS via the CNRS-Univ. of Chicago agreement. RC acknowledges financial support from the European Research Council under EU Horizon 2020 research and innovation program (ERC IMPACT grant agreement 681818), the project VADIS, financed by the LABEX UnivEarths of the University Paris Cite, the project HIDDEN (no. 223272) of the Research Council of Norway, and sigma2/notur via project no. NN9697K. This work was performed using eDARI HPC resources from GENCI, IDRIS, and TGCC via Grant series no. 906368. We acknowledge access to the PSMN supercomputer at ENS Lyon. This research has made use of the NASA Exoplanet Archive, which is operated by the California Institute of Technology, under contract with the National Aeronautics and Space Administration under the Exoplanet Exploration Program.

## References

Alfe, D., Kresse, G., & Gillan, M. J. (2000). Structure and dynamics of liquid iron under Earth's core conditions. *Physical Review B*, *61*(1), 132–142. https://doi.org/10.1103/PhysRevB.61.132

Blöchl, P. E. (1994). Projector augmented-wave method. *Physical Review B*, *50*(24), 17953–17979. https://doi.org/10.1103/PhysRevB.50.17953

Broadley, M. W., Bekaert, D. V., Piani, L., Füri, E., & Marty, B. (2022). Origin of life-forming volatile elements in the inner Solar System. *Nature*, *611*(7935), 245–255. https://doi.org/10.1038/s41586-022-05276-x

Buffett, B. A. (2000). Earth's core and the Geodynamo. *Science*, *288*(5473), 2007–2012. https://doi.org/10.1126/science.288.5473.2007

Caracas, R. (2015). The influence of hydrogen on the seismic properties of solid iron. *Geophysical Research Letters*, *42*(10), 3780–3785. https://doi.org/10.1002/2015GL063478

Caracas, R., Kobsch, A., Solomatova, N. V., Li, Z., Soubiran, F., & Hernandez, J. A. (2021). Analyzing melts and fluids from ab initio molecular dynamics simulations with the UMD package. *Journal of Visualized Experiments*, *175*, e61534. https://doi.org/10.3791/61534

Ciesla, F., & Lauretta, D. (2005). Radial migration and dehydration of phyllosilicates in the solar nebula. *Earth and Planetary Science Letters*, *231*(1–2), 1–8. https://doi.org/10.1016/j.epsl.2004.12.022

de Wijs, G. A., Kresse, G., Vočadlo, L., Dobson, D., Alfe, D., Gillan, M. J., & Price, G. D. (1998). The viscosity of liquid iron at the physical conditions of the Earth's core. *Nature*, *392*(6678), 805–807. https://doi.org/10.1038/33905

Dziewonski, A. M., & Anderson, D. L. (1981). Preliminary reference Earth model. *Physics of the Earth and Planetary Interiors*, *25*(4), 297–356. https://doi.org/10.1016/0031-9201(81)90046-7

Fu, S., Chariton, S., Prakapenka, V. B., & Shim, S. H. (2023). Core origin of seismic velocity anomalies at Earth's core–mantle boundary. *Nature*, *615*(7953), 646–651. https://doi.org/10.5281/zenodo.7413050

Fukai, Y., & Suzuki, T. (1986). Iron-water reaction under high pressure and its implication in the evolution of the Earth. *Journal of Geophysical Research*, *91*(B9), 9222–9230. https://doi.org/10.1029/JB091iB09p09222

Hirose, K., Tagawa, S., Kuwayama, Y., Sinmyo, R., Morard, G., Ohishi, Y., & Genda, H. (2019). Hydrogen limits carbon in liquid iron. *Geophysical Research Letters*, *46*(10), 5190–5197. https://doi.org/10.1029/2019GL082591

Hirose, K., Wood, B., & Vočadlo, L. (2021). Light elements in the Earth's core. *Nature Reviews Earth & Environment*, *2*(9), 645–658. https://doi.org/10.1038/s43017-021-00203-6

Hoover, W. G. (1985). Canonical dynamics: Equilibrium phase-space distributions. *Physical Review A*, *31*(3), 1695–1697. https://doi.org/10.1103/PhysRevA.31.1695

Ichikawa, H., Tsuchiya, T., & Tange, Y. (2014). The P-V-T equation of state and thermodynamic properties of liquid iron. *Journal of Geophysical Research: Solid Earth*, *119*(1), 240–252. https://doi.org/10.1002/2013JB010732

Iizuka-Oku, R., Yagi, T., Gotou, H., Okuchi, T., Hattori, T., & Sano-Furukawa, A. (2017). Hydrogenation of iron in the early stage of Earth's evolution. *Nature Communications*, *8*(1), 14096. https://doi.org/10.1038/ncomms14096

Irving, J. C., Cottaar, S., & Lekić, V. (2018). Seismically determined elastic parameters for Earth's outer core. *Science Advances*, *4*(6), eaar2538. https://doi.org/10.1126/sciadv.aar2538

Irving, J. C., Lekić, V., Durán, C., Drilleau, M., Kim, D., Rivoldini, A., et al. (2023). First observations of core-transiting seismic phases on Mars. *Proceedings of the National Academy of Sciences*, *120*(18), e2217090120. https://doi.org/10.1073/pnas.2217090120

Jaupart, E., Charnoz, S., & Moreira, M. (2017). Primordial atmosphere incorporation in planetary embryos and the origin of Neon in terrestrial planets. *Icarus*, *293*, 199–205. https://doi.org/10.1016/j.icarus.2017.04.022

Jones, C. A., & Schubert, G. (2015). Thermal and compositional convection in the outer core. *Treatise in Geophysics, Core Dynamics*, *8*, 131–185. https://doi.org/10.1016/b978-044452748-6/00130-9

Kresse, G., & Furthmüller, J. (1996). Efficient iterative schemes for ab initio total-energy calculations using a plane-wave basis set. *Physical Review B*, *54*(16), 11169–11186. https://doi.org/10.1103/PhysRevB.54.11169

Li, Y., Guo, X., Vočadlo, L., Brodholt, J. P., & Ni, H. (2022). The effect of water on the outer core transport properties. *Physics of the Earth and Planetary Interiors*, *329*, 106907. https://doi.org/10.1016/j.pepi.2022.106907

Li, Y., Vočadlo, L., Sun, T., & Brodholt, J. P. (2020). The Earth's core as a reservoir of water. *Nature Geoscience*, *13*(6), 453–458. https://doi.org/10.5285/d0677edf-c987-497d-aae8-23bf22ef774d

Li, Z., & Caracas, R. (2021). Thermophysical properties of hot fluid iron in the protolunar disk. *Physics of the Earth and Planetary Interiors*, *321*, 106806. https://doi.org/10.1016/j.pepi.2021.106806

Lou, H., Wang, X., Cao, Q., Zhang, D., Zhang, J., Hu, T., et al. (2013). Negative expansions of interatomic distances in metallic melts. *Proceedings of the National Academy of Sciences*, *110*(25), 10068–10072. https://doi.org/10.1073/pnas.1307967110

Nosé, S. (1984). A unified formulation of the constant temperature molecular dynamics methods. *The Journal of chemical physics*, *81*(1), 511–519. https://doi.org/10.1063/1.447334

O'Brien, D. P., Walsh, K. J., Morbidelli, A., Raymond, S. N., & Mandell, A. M. (2014). Water delivery and giant impacts in the "Grand Tack" Scenario. *Icarus*, *239*, 74–84. https://doi.org/10.1016/j.icarus.2014.05.009

Ohmura, S., Tsuchiya, T., & Shimojo, F. (2020). Structures of liquid iron–light-element mixtures under high pressure. *Physica Status Solidi*, *257*(11), 2000098. https://doi.org/10.1002/pssb.202000098

Oka, K., Ikuta, N., Tagawa, S., Hirose, K., & Ohishi, Y. (2022). Melting experiments on Fe-O-H and Fe-H: Evidence for eutectic melting in Fe-FeH and implications for hydrogen in the core. *Geophysical Research Letters*, *49*(17), e2022GL099420. https://doi.org/10.1029/2022GL099420

Okuchi, T. (1997). Hydrogen partitioning into molten iron at high pressure: Implications for Earth's core. *Science*, *278*(5344), 1781–1784. https://doi.org/10.1126/science.278.5344.1781

Olson, P. L., & Sharp, Z. D. (2019). Nebular atmosphere to Magma Ocean: A model for volatile capture during Earth accretion. *Physics of the Earth and Planetary Interiors*, *294*, 106294. https://doi.org/10.1016/j.pepi.2019.106294

Perdew, J. P., Burke, K., & Ernzerhof, M. (1996). Generalized gradient approximation made simple. *Physical Review Letters*, *77*(18), 3865–3868. https://doi.org/10.1103/PhysRevLett.77.3865

Posner, E. S., & Steinle-Neumann, G. (2019). Mass transport and structural properties of binary liquid iron alloys at high pressure. *Geochemistry, Geophysics, Geosystems*, *20*(7), 3556–3568. https://doi.org/10.1029/2019GC008393

Raymond, S. N., O'Brien, D. P., Morbidelli, A., & Kaib, N. A. (2009). Building the terrestrial planets: Constrained accretion in the inner Solar System. *Icarus*, *203*(2), 644–662. https://doi.org/10.1016/j.icarus.2009.05.016

Seager, S., Kuchner, M., Hier-Majumder, C. A., & Militzer, B. (2007). Mass-radius relationships for solid exoplanets. *The Astrophysical Journal*, *669*(2), 1279–1297. https://doi.org/10.1086/521346

Stimpfl, M., Walker, A. M., Drake, M. J., de Leeuw, N. H., & Deymier, P. (2006). An ångström-sized window on the origin of water in the inner solar system: Atomistic simulation of adsorption of water on olivine. *Journal of Crystal Growth*, *294*(1), 83–95. https://doi.org/10.1016/j.jcrysgro.2006.05.057

Stoutenburg, E. R. (2024). Equation of state, structure, and transport properties of iron hydride melts at planetary interior conditions [Dataset]. *Zenodo*. https://doi.org/10.5281/zenodo.10083811

Suzuki, T., Akimoto, S. I., & Fukai, Y. (1984). The system iron-enstatite-water at high pressures and temperatures—Formation of iron hydride and some geophysical implications. *Physics of the Earth and Planetary Interiors*, *36*(2), 135–144. https://doi.org/10.1016/0031-9201(84)90014-1

Tagawa, S., Sakamoto, N., Hirose, K., Yokoo, S., Hernlund, J., Ohishi, Y., & Yurimoto, H. (2021). Experimental evidence for hydrogen incorporation into Earth's core. *Nature Communications*, *12*(1), 2588. https://doi.org/10.1038/s41467-021-22035-0

Thompson, E. C., Davis, A. H., Bi, W., Zhao, J., Alp, E. E., Zhang, D., et al. (2018). High-pressure geophysical properties of Fcc phase $FeH_x$. *Geochemistry, Geophysics, Geosystems*, *19*(1), 305–314. https://doi.org/10.1002/2017GC007168

Umemoto, K., & Hirose, K. (2015). Liquid iron-hydrogen alloys at outer core conditions by first-principles calculations. *Geophysical Research Letters*, *42*(18), 7513–7520. https://doi.org/10.1002/2015GL065899

Young, E. D., Shahar, A., & Schlichting, H. E. (2023). Earth shaped by primordial $H_2$ atmospheres. *Nature*, *616*(7956), 306–311. https://doi.org/10.1038/s41586-023-05823-0

Yuan, L., & Steinle-Neumann, G. (2020). Strong sequestration of hydrogen into the Earth's core during planetary differentiation. *Geophysical Research Letters*, *47*(15), e2020GL088303. https://doi.org/10.1029/2020GL088303

Zeng, L., & Seager, S. (2008). A computational tool to interpret the bulk composition of solid exoplanets based on mass and radius measurements. *Publications of the Astronomical Society of the Pacific*, *120*(871), 983–991. https://doi.org/10.1086/591807

Zhang, Y., Guo, G., & Nie, G. (2000). A molecular dynamics study of bulk and shear viscosity of liquid iron using embedded-atom potential. *Physics and Chemistry of Minerals*, *27*(3), 164–169. https://doi.org/10.1007/s002690050004

Zong, H., Wiebe, H., & Ackland, G. J. (2020). Understanding high pressure molecular hydrogen with a hierarchical machine-learned potential. *Nature Communications*, *11*(1), 5014. https://doi.org/10.1038/s41467-020-18788-9